Journal of Materials Processing Technology 217 (2015) 1–12

Contents lists available at ScienceDirect

Journal of Materials Processing Technology

journal homepage: www.elsevier.com/locate/jmatprotec

Deformation and recrystallization of single crystal nickel-based superalloys during investment casting

Li Zhonglin [a], Xiong Jichun [b], Xu Qingyan [a,*], Li Jiarong [b], Liu Baicheng [a]

[a] School of Materials Science and Engineering, Key Laboratory for Advanced Materials Processing Technology, Ministry of Education, Tsinghua University, Beijing 100084, China

[b] National Key Laboratory of Advanced High Temperature Structural Materials, Beijing Institute of Aeronautical Materials, Beijing 100095, China

ARTICLE INFO

Article history:
Received 28 August 2014
Received in revised form 21 October 2014
Accepted 23 October 2014
Available online 4 November 2014

Keywords:
Single crystal
Superalloys
Investment casting
Plastic deformation
Recrystallization

ABSTRACT

A semi-quantitative, macroscopic, phenomenon-based, thermo-elastic–plastic model was developed to predict the final plastic strains of single crystal nickel-based superalloys by considering their orthotropic mechanical properties. Various cases were considered and simulated to investigate the basic factors that influence the final plasticity. Thermo-mechanical numerical analysis was conducted to predict the recrystallization sites of simplified cored rods, with the results in good agreement with the experimental results. These hollowed rods with thin walls showed an increased propensity for recrystallization. The geometric features, especially stress concentration sites, are more significant to the induced plasticity than the material's orientation or shell/core materials. This paper also attempts to provide useful suggestions, such as introducing filets, to avoid causing plastic strains during the casting process that induce recrystallization.

1. Introduction

Turbine blades for gas turbine applications are fabricated by investment casting, often in single crystal form, which can allow higher inlet gas temperatures to be used and increase efficiency. However, the external and internal geometries of single crystal blades are becoming increasingly complicated, making them more difficult to cast as greater care is required to prevent defects, such as stray grains and freckles, being introduced during the manufacturing process. Recrystallization (RX) is one of the major difficulties and can be ascribed to plastic deformation, as demonstrated by Burgel et al. (2000). During the manufacture of new parts, plastic deformation can be caused by several possible sources: thermal contraction during solidification and subsequent cooling, removing the ceramic mold and core material mechanically, stamping identification marks, grinding the airfoil, etc. In practice, plastic deformation will induce RX during subsequent heat treatments or long-term service. For example, RX can introduce high-angle grain boundaries, which are obviously undesirable. As demonstrated by Meng et al. (2010) and Moverare et al. (2009), RX is potentially detrimental to creep and fatigue properties, respectively.

Work has been done to study the phenomenon of RX in single crystal nickel-based superalloys. Some research has focused on the influence of microstructural features on RX, such as γ′-precipitates, carbides, and γ/γ′ eutectics. For example, Dahlen and Winberg (1980) have discussed the influence of γ′-precipitation on the RX of nickel-based superalloys. Wang et al. (2013) and Xiong et al. (2010) have investigated the effect of carbon content on the RX of single crystal (SX) nickel-based superalloys. In addition, Wang et al. (2009) studied the influence of eutectics on plastic deformation and the subsequent RX of the SX nickel-based superalloy CMSX-4. Meanwhile, some research has concentrated on the effect of different annealing conditions and crystallographic orientations on RX behavior. Wu et al. (2012) conducted surface RX of a Ni_3Al-based SX superalloy at different annealing temperatures and blasting pressures. Xie et al. (2012) studied the crystallographic orientation dependence of RX in a Ni-based SX superalloy. However, little attention has been paid to the effect of geometric features, ceramic shell and core material, and processing details. Certain critical questions need to be answered, such as at what temperature will RX occur? What is the critical plastic deformation required to induce RX?, and what is the influence of the geometric features, including holes and platforms? Answers to these questions will allow more efficient foundry processes, even process-friendly blade designs, to be developed. Modeling has been used to analyze the directional

* Corresponding author. Tel.: +86 10 62795482; fax: +86 10 62773637.
E-mail addresses: lzl07@mails.tsinghua.edu.cn (Z. Li), jichunxiong@gmail.com (J. Xiong), scjxqy@tsinghua.edu.cn (Q. Xu), jiarong.li@biam.ac.cn (J. Li), liubc@mail.tsinghua.edu.cn (B. Liu).

http://dx.doi.org/10.1016/j.jmatprotec.2014.10.019

solidification of SX superalloys from thermal and microstructural perspectives. Pan et al. (2010) conducted multiscale modeling and simulations of the directional solidification process of turbine blade casting, which resulted in good predictions of temperature profiles and grain number. Dai et al. (2011) investigated grain selection in spiral selectors during investment casting of SX turbine blades through both experimental and numerical modeling techniques. One advantage simulation provides over experiments is that it can predict the plastic strains that cause RX.

The overarching goal of this study was to build a physics-based tool for predicting casting-induced plasticity and subsequent RX during the heat treatment of SX superalloys by considering the material's anisotropic mechanical properties. Panwisawas et al. (2013a,b) developed a mathematical model to predict plasticity and RX in investment-cast SX superalloys. However, this model considered SX superalloys as isotropic materials, which does not conform to the reality. Many mechanical models have been proposed to describe the mechanical properties of anisotropic materials. Ding et al. (2004) proposed a macroscopic phenomenon-based model built on a modified Hill plasticity model. Zambaldi et al. (2007) employed a microscopic crystal plasticity model, which was built on the physical deformation mechanisms of materials, to predict the distribution of crystallographic slip in SX nickel-based superalloys. The former gained great popularity for its concise equations, as well as its convenience and speed of calculations, though the latter model can give more accurate predictions of slips and grain size.

This paper proposed a mathematical thermo-mechanical model using the Hill's plasticity model as a basis, which considers the orthotropic mechanical properties of SX superalloys, and took into account both the scale effect and convenience. Numerical analysis using this model was performed to identify the major factors that cause the plasticity during investment casting and RX during the subsequent heat treatment. A series of simplified thermo-mechanical numerical analyses with the DD6 superalloy were conducted and compared with experimental results to test the validity of the model. This model could be employed to optimize processing conditions to reduce the likelihood of RX.

2. Mathematical model of SX superalloys

Plastic deformation during investment casting mainly occurs because of the different thermal expansion coefficients of the metals, and the ceramic shell and core. Assuming the plasticity is rate-independent, the thermal strain (ε_{th}), elastic strain (ε_{el}), and plastic strain (ε_{pl}) follow the relation below:

$$\varepsilon_{th} + \varepsilon_{el} + \varepsilon_{pl} = 0 \tag{1}$$

The thermal strain can be calculated as

$$\varepsilon_{th} = \alpha \Delta T = \alpha (T - T_{ref}) \tag{2}$$

Here, T_{ref} is the reference temperature, which is usually room temperature. The variable α denotes the thermal expansion coefficient, which is usually considered isotropic for SX materials (Green, 1998).

2.1. Orthotropic elastic properties

The elastic strain part of the model for SX superalloys considers the orthotropic characteristics. For materials with cubic structures (BCC or FCC), where the three principal orientations (denoted 1, 2, and 3) are identical, the elastic constitutive equation is determined with the generalized Hooke law, which can be expressed as follows:

$$\begin{aligned} &\{\varepsilon\} = [S]\{\sigma\} \\ &\{\sigma\} = [S]^{-1}\{\varepsilon\} = [C]\{\varepsilon\} \end{aligned} \tag{3}$$

$$\begin{aligned} &\{\varepsilon\} = [\varepsilon_{11}\varepsilon_{22}\varepsilon_{33}\gamma_{12}\gamma_{23}\gamma_{31}]^T \\ &\{\sigma\} = [\sigma_{11}\sigma_{22}\sigma_{33}\tau_{12}\tau_{23}\tau_{31}]^T \\ &[S] = [C]^{-1} \end{aligned} \tag{4}$$

$$[S] = \begin{pmatrix} 1/E & -\mu/E & -\mu/E & 0 & 0 & 0 \\ -\mu/E & 1/E & -\mu/E & 0 & 0 & 0 \\ -\mu/E & -\mu/E & 1/E & 0 & 0 & 0 \\ 0 & 0 & 0 & 1/G & 0 & 0 \\ 0 & 0 & 0 & 0 & 1/G & 0 \\ 0 & 0 & 0 & 0 & 0 & 1/G \end{pmatrix} \tag{5}$$

where $\{\sigma\}$ and $\{\varepsilon\}$ are the stress and strain vectors, respectively. S_{ij} and C_{ij} denote the elastic compliance and stiffness constants, respectively, which measure the strain (or stress) necessary to maintain a given stress (or strain). E, μ, and G are the Young's modulus, Poisson's ratio, and shear modulus, respectively, in the three principal orientations: ⟨0 0 1⟩, ⟨0 1 0⟩, and ⟨1 0 0⟩. The stiffness and compliance constants have the following relations:

$$S_{11} = \frac{C_{11} + C_{12}}{(C_{11} - C_{12})(C_{11} + 2C_{12})} \tag{6}$$

$$S_{12} = \frac{C_{12}}{(C_{11} - C_{12})(C_{11} + 2C_{12})} \tag{7}$$

$$S_{44} = \frac{1}{C_{44}} \tag{8}$$

The matrix phase, γ, and precipitate phase, γ′, both exhibit FCC structures and have coherent interfaces. Therefore, the nickel-based SX superalloys can be considered approximately orthotropic materials with three identical principal orientations. There are only 3 independent constants in $[S]$.

By applying spatial geometry transformations, the Young's modulus, E', and shear modulus, G', in a given crystallographic orientation can be obtained as follows:

$$\frac{1}{E'} = S'_{11} = S_{11} - 2JS\left(\frac{S_{11} - S_{12} - S_{44}}{2}\right) \tag{9}$$

with the orientation parameters J and S given by:

$$J = l^2m^2 + l^2n^2 + m^2n^2 \tag{10}$$

$$S = 2S_{11} - 2S_{12} - S_{44} \tag{11}$$

where l, m, and n represent the directional cosines relative to the axes 1, 2, and 3, respectively. Thus, the degree of anisotropy depends on the orientation parameter, which has a minimum value of zero along ⟨0 0 1⟩, a maximum value of 1/3 along ⟨1 1 1⟩, and a value of 1/4 along ⟨0 1 1⟩. For a pure nickel SX at room temperature, typical values for the compliance constants are $S_{11} = 0.799 \times 10^{-5}\,\mathrm{MPa}^{-1}$, $S_{12} = -0.312 \times 10^{-5}\,\mathrm{MPa}^{-1}$, and $S_{44} = 0.844 \times 10^{-5}\,\mathrm{MPa}^{-1}$. It can be seen that the ⟨1 0 0⟩ direction is the least stiff, while the ⟨1 1 1⟩ direction is the stiffest, with ⟨1 1 0⟩ between these two limits. The values of Young's modulus along these crystallographic orientations are $E_{\langle 0\,0\,1\rangle} = 125$ GPa, $E_{\langle 0\,1\,1\rangle} = 220$ GPa, and $E_{\langle 1\,1\,1\rangle} = 294$ GPa. SX superalloys display a similar degree of anisotropy. To determine the degree of elastic anisotropy in SX cubic materials, the anisotropic factor, A, is defined as:

$$A = \frac{2C_{44}}{C_{11} - C_{12}} = \frac{2(S_{11} - S_{12})}{S_{44}} \tag{12}$$

where $A = 1$ for isotropic materials. For example, the following cubic metals have A values of 2.44 (Ni), 3.19 (Cu), 2.97 (Ag), 2.90 (Au), 1.65 (Ge), and 1.22 (Al). Thus, Ni displays a fair degree of anisotropy, but it is not the most anisotropic cubic metal.

The Young's and shear moduli over a wide range of temperature can be obtained using many methods, with tensile testing and

dynamic resonance techniques most widely used for their simple principles and high accuracy. The Poisson's ratio at low or high temperatures can be measured with Moire interferometry.

Fig. 1 shows the variation of the Young's and shear moduli for different SX nickel-based superalloys with crystallographic orientation and temperature. The moduli of DD6 were measured by tensile tests, with the values for all other alloys measured with dynamic resonance techniques. Bayerlein and Sockel (1992) provided data for MA760 and IN738LC, while the data for CMSX4, SRR99, and SX pure Ni are from Fahrmann et al. (1999), Hermann and Han (1996), and Reed (2006), respectively. It can be seen that the moduli between different SX superalloy systems are relatively close, and all decrease with increasing temperature, especially above 950 °C.

2.2. Plastic behavior

For anisotropic materials, the Hill yield criterion, which is a simple extension of the von Mises criterion, is usually employed.

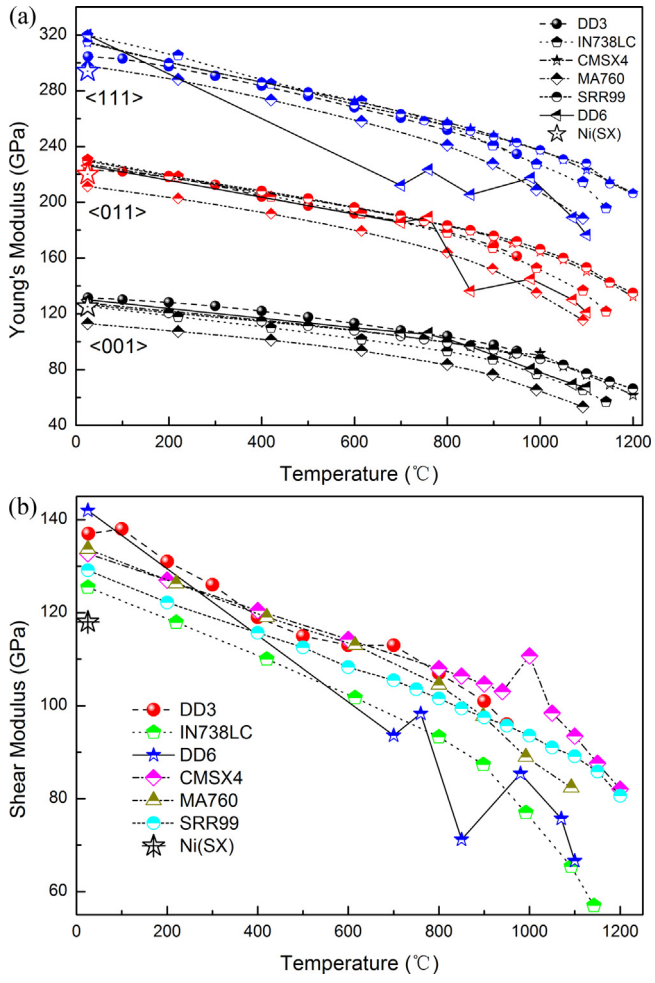

Fig. 1. Variation of the measured Young's and shear moduli of some SX Ni-based superalloys with crystallographic orientation and temperature (data of MA760, IN738LC, CMSX4 and SRR99 from literature, and data of DD3 and DD6 from the handbook).

Hill's potential function expressed in terms of rectangular Cartesian stress components has the following form:

$$f(\sigma) = \sqrt{F(\sigma_{22}-\sigma_{33})^2 + G(\sigma_{33}-\sigma_{11})^2 + H(\sigma_{11}-\sigma_{22})^2 + 2L\sigma_{23}^2 + 2M\sigma_{31}^2 + 2N\sigma_{12}^2} \quad (13)$$

where F, G, H, L, M, and N are independent constants obtained from tensile or compression tests of the material in different orientations. If $f(\boldsymbol{\sigma}) > \sigma_0$, the material will yield, where σ_0 is the user-defined reference yield stress specified for the metal plasticity definition, usually the yield strength in one principal orientation. In this article, $\sigma_0 = S_{\langle 0\,0\,1\rangle}$, where $S_{\langle 0\,0\,1\rangle}$ indicates the yield strength in one principal orientation. The mechanical properties are identical in the three principal orientations for FCC materials, and hence, $f(\boldsymbol{\sigma})$ can be expressed as:

$$f(\sigma) = \frac{1}{\sqrt{2}}\sqrt{(\sigma_{22}-\sigma_{33})^2 + (\sigma_{33}-\sigma_{11})^2 + (\sigma_{11}-\sigma_{22})^2 + 2K(\sigma_{23}^2+\sigma_{31}^2+\sigma_{12}^2)} \quad (14)$$

where $K = L/F$ and denotes the anisotropic plastic parameter. This potential function will take the form of the von Mises criterion if $K = 3$, meaning that the material is isotropic. Theoretically, the yield stresses $S_{\langle 0\,0\,1\rangle}$, $S_{\langle 0\,1\,1\rangle}$, and $S_{\langle 1\,1\,1\rangle}$ obtained through uniaxial tests have the following relations:

$$S_{\langle 1\,1\,1\rangle} = \left(\frac{K}{3}\right)^{1/2} S_{\langle 0\,0\,1\rangle} \quad (15)$$

$$S_{\langle 0\,1\,1\rangle} = \frac{1}{2}(1+K)^{1/2} S_{\langle 0\,0\,1\rangle} \quad (16)$$

Isotropic hardening criterion is employed for this model, with the flow rule used in this model as follows:

$$d\varepsilon^{pl} = d\lambda \frac{\partial f}{\partial \boldsymbol{\sigma}} = \frac{d\lambda}{f}\boldsymbol{b} \quad (17)$$

where λ denotes the plastic multiplier. From the above definition of $f(\boldsymbol{\sigma})$, $\boldsymbol{b}$ can be expressed as:

$$\boldsymbol{b} = \begin{bmatrix} \sigma_{11} - 0.5(\sigma_{22}+\sigma_{33}) \\ \sigma_{22} - 0.5(\sigma_{11}+\sigma_{33}) \\ \sigma_{33} - 0.5(\sigma_{11}+\sigma_{22}) \\ K\sigma_{12} \\ K\sigma_{31} \\ K\sigma_{23} \end{bmatrix} \quad (18)$$

2.3. Validation of orthotropic mechanical properties

Validation of a mathematical model is very significant for modeling and simulation. This subsection will show the calculation of some critical mechanical parameters that were used in the simulations. Experimental data was used in the calculations to verify and validate the use of orthotropic mechanical properties.

Several methods have been developed to determine the elastic constants from measured moduli and Poisson's ratios. Hermann and Han (1996) developed the regression method, which is the simplest way to determine the elastic compliance constants. This method is based on Eqs. (9)–(11). The reciprocal values of the measured moduli, E^{-1}, for different orientations can be plotted against the orientation parameter, J. Plotting the reciprocal values of shear modulus will allow the elastic constant S_{44} to be determined. A linear regression with $J = 0$ results in the calculation of elastic constant S_{11}, while S_{12} can be calculated with Eq. (11) from the slope of the regression lines. The slope of regression lines from plots of measured reciprocal elastic moduli against J is equal to $-2S$, as shown in Fig. 2. Therefore, the elastic compliance constants can be easily obtained with this method, as Young's and shear moduli in a

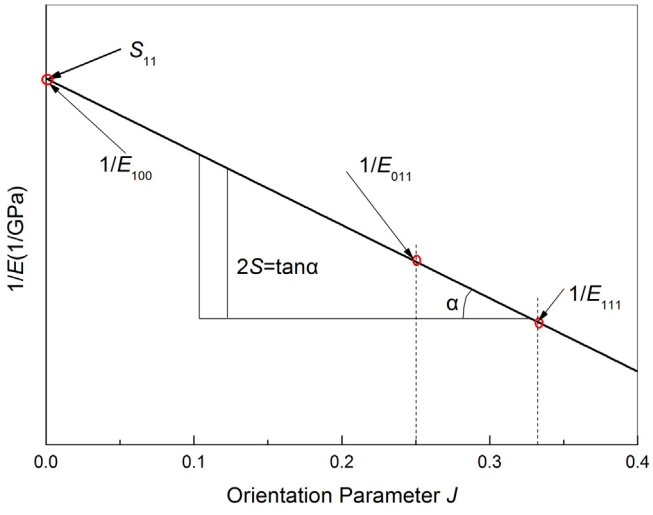

Fig. 2. Schematic of the regression method used to determine elastic compliance constants.

given orientation can be measured experimentally. In addition, the more values obtained for moduli in various orientations, the more accurate the calculated compliance constants.

Sometimes Poisson's ratios are measured and reported instead of the shear modulus. In this case, the shear modulus can be calculated with another method, which will be illustrated next. By combining Eqs. (5) and (9) along ⟨1 1 0⟩ and ⟨1 1 1⟩, the following relations can be obtained:

$$\frac{1}{G} = \frac{3}{E_{1\,1\,1}} - \frac{1-2\mu}{E} \tag{19}$$

$$\frac{1}{G} = \frac{4}{E_{1\,1\,0}} - \frac{2-2\mu}{E} \tag{20}$$

Through Eqs. (14) and (15), the shear moduli G_1 and G_2 can be obtained, respectively. For the model, the shear modulus, G, is the average of G_1 and G_2:

$$G = \frac{G_1 + G_2}{2} \tag{21}$$

Figs. 3 and 4 show the compliance constants and anisotropic elastic factors of different SX superalloys obtained with the regression method. As the temperature increases, the stiffness of the materials decreases, especially above 950 °C. Combining Eqs. (9) and (11), Young's moduli in all orientations can be determined, as shown in Fig. 5. Table 1 compares the calculated results from the regression plots and measured values of Young's moduli of the SX superalloy DD6. As shown by the similarity of the calculated and measured results, it is acceptable to use calculations based on orthotropic elastic properties in the model.

Using Eq. (15), the parameter K can be calculated using the yield strength and ultimate tensile strength, denoted K_p and K_b, respectively. For ease of calculation, the average of K_p and K_b is taken as the calculated anisotropic plastic parameter. For the SX superalloy DD6, the values of $S_{\langle 0\,1\,1\rangle}$ and ultimate tensile strength ($UTS_{\langle 0\,1\,1\rangle}$)

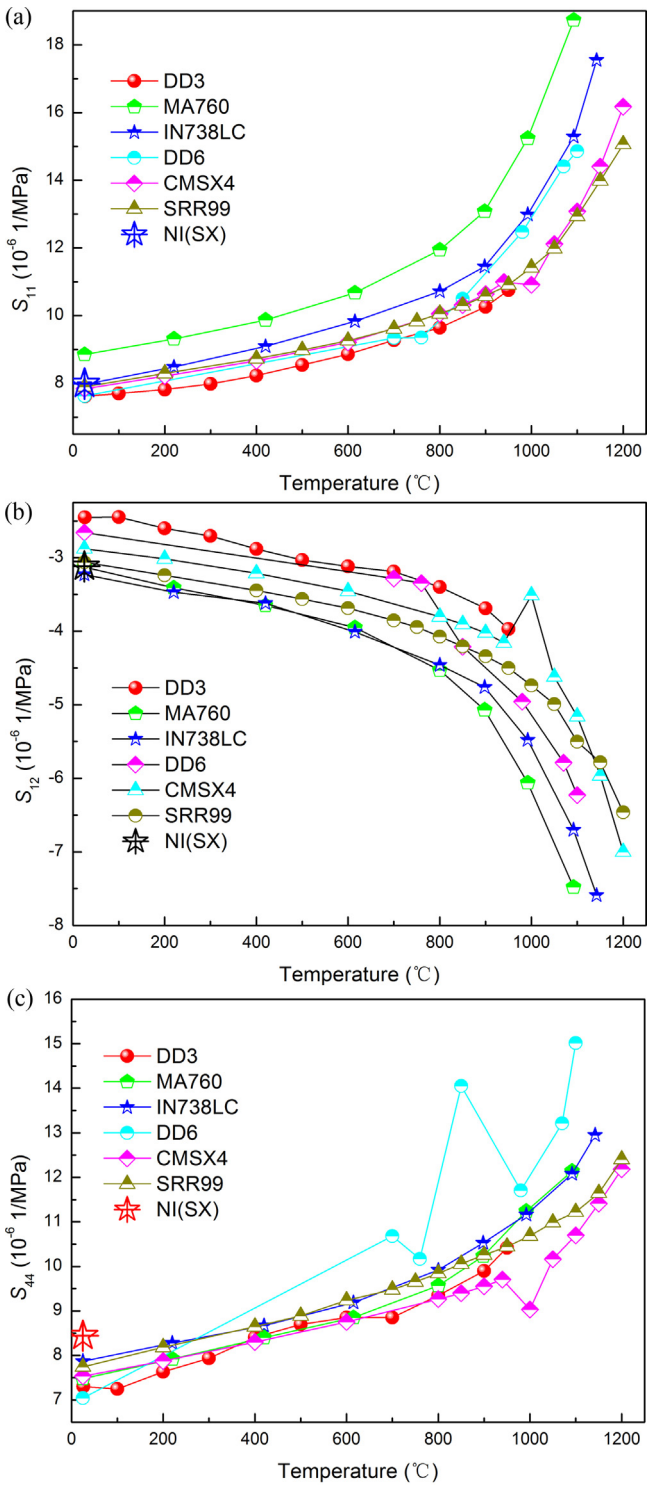

Fig. 3. Variation of elastic compliance constants for different SX Ni-based superalloys with temperature. The data was calculated with the regression method.

Table 1
Variation of calculation value and errors of Young's modulus in ⟨0 0 1⟩, ⟨0 1 1⟩ and ⟨1 1 1⟩ with different temperatures.

Temperature (°C)	25	700	760	850	980	1070	1100
Calculation value of $E_{\langle 0\,0\,1\rangle}$ (GPa)	131.2	107.1	107	95.2	80.2	69.4	67.3
Calculation value of $E_{\langle 0\,1\,1\rangle}$ (GPa)	235.7	175.5	180.4	150.2	149.6	131.3	123.9
Calculation value of $E_{\langle 1\,1\,1\rangle}$ (GPa)	320.9	223	233.9	186	210.3	186.9	172.1
Error of $E_{\langle 0\,0\,1\rangle}$	−0.25%	0.82%	0.71%	−1.62%	−0.42%	−0.14%	−0.32%
Error of $E_{\langle 0\,1\,1\rangle}$	1.81%	−5.39%	−4.82%	10.21%	3.15%	10.26%	2.37%
Error of $E_{\langle 1\,1\,1\rangle}$	−1.85%	5.14%	4.69%	−9.48%	−3.33%	−1.10%	−2.47%

Table 2
Variation of the anisotropic parameter K and calculation error of $S_{\langle 0\,1\,1\rangle}$ and $UTS_{\langle 0\,1\,1\rangle}$ with different temperatures.

Temperature (°C)	25	700	760	850	980	1070	1100
Anisotropic plastic parameter K	6.2	3.47	3.44	2.46	1.87	2.15	2.36
Calculation error of $S_{\langle 0\,1\,1\rangle}$	34.20%	–	–	–	−2.40%	−13.20%	−10.70%
Calculation error of $UTS_{\langle 0\,1\,1\rangle}$	26.30%	11.10%	13.60%	−1.50%	−5.90%	−9.60%	5.30%

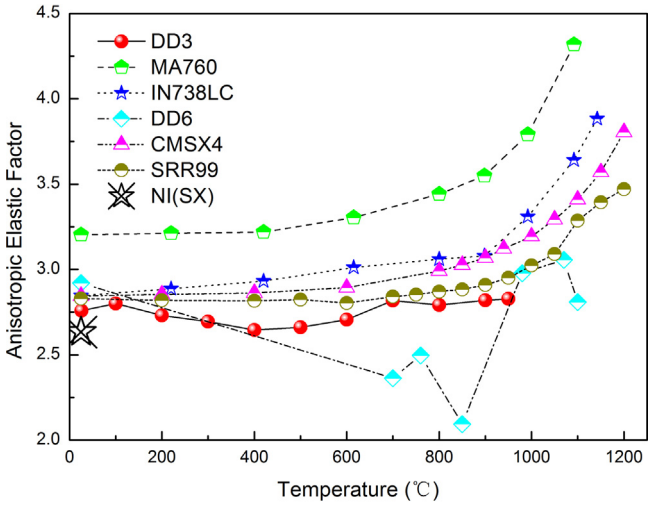

Fig. 4. Variation of anisotropic elastic factors for some SX Ni-based superalloys with temperature. The data was calculated using Eq. (12).

predicted with the calculated K were compared with the experimental results, as shown in Table 2. It reveals that the calculated yield strength and ultimate tensile strength in the ⟨0 1 1⟩ direction are fairly accurate for temperatures of 850 °C and 980 °C. The Hill's yield criterion is acceptable when modeling above 700 °C, which is the temperature range this model is most concerned with.

It should be noted that the difference between the measured and calculated values for the elastic and plastic properties is not only from the measurement error, but also an inherent characteristic of engineered SX superalloys. Though the matrix and precipitate phases both exhibit FCC structures, all SX superalloys are not ideal orthotropic materials in reality. Therefore, orthotropic elastic theory and Hill's yield criterion are unable to fully describe the elastic and plastic behavior of SX nickel-based superalloys. However, to some extent, they are valid for semi-quantitative analysis from an engineering perspective.

3. Experimental

3.1. Directional solidification

A simplified cored rod geometry was designed for investigating RX. Fig. 6 illustrates the geometric details of the test pieces, which

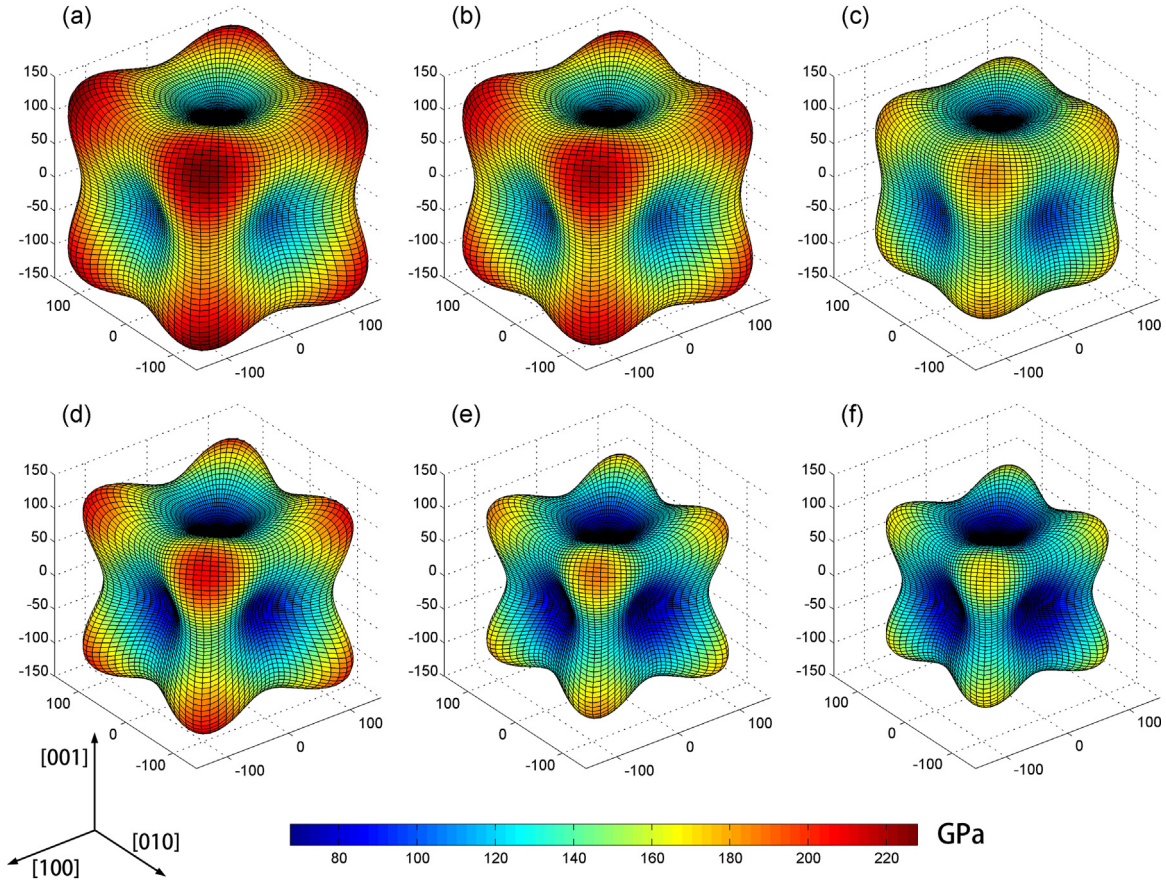

Fig. 5. Orientation and temperature dependence of Young's modulus of SX superalloy DD6: (a) 700 °C; (b) 760 °C; (c) 850 °C; (d) 980 °C; (e) 1070 °C; (f) 1100 °C.

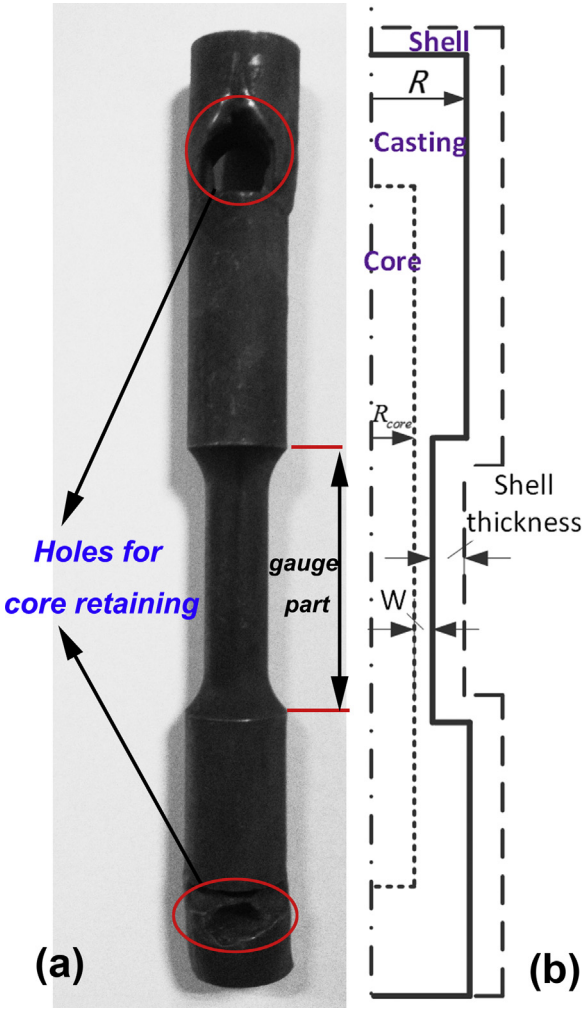

Fig. 6. Typical geometry of a test piece: (a) cored casting and (b) schematic of the geometry, where R_{core}, R, and W denote core radius, platform radius, and wall thickness, respectively.

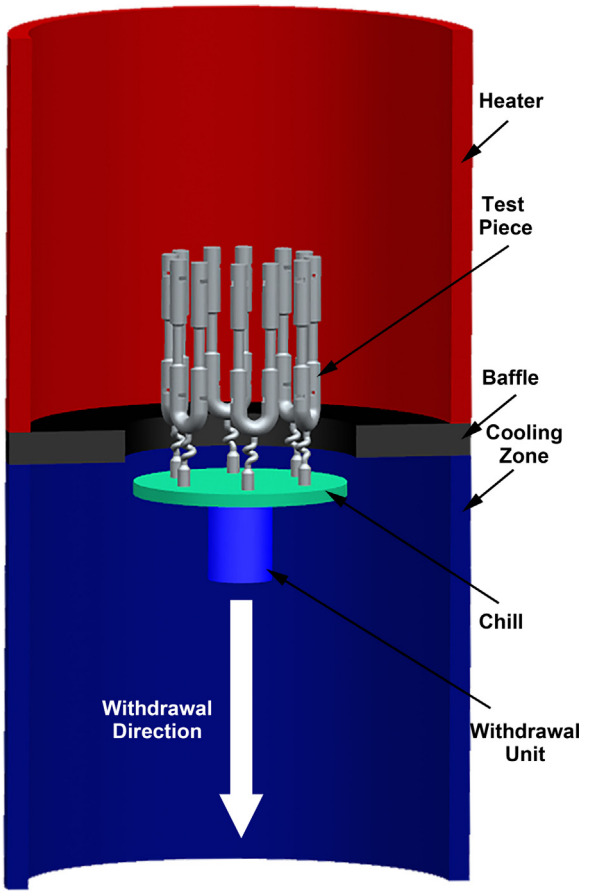

Fig. 7. Schematic of the directional solidification process with the configuration of test pieces cast.

are analogs of comparable size to a turbine blade aerofoil, with flanges to simulate the mechanical constraints provided by platforms and shrouds, as well as ceramic molds. Holes on both ends were created for core retaining. The gauge's length was 40 mm, with a diameter of 10 mm and a casting wall thickness of about 1.5 mm. Filets with radii of 3 mm were introduced where abrupt changes in section occurred. The nominal thickness of the shell was approximately 5 mm. The second generation SX superalloy DD6 was used for the experiments. The composition of DD6 is given in Table 3. The material exhibits a two-phase microstructure, with coherent and cuboidal γ′-precipitates that are surrounded by the γ-matrix. The cored rods were fabricated using an industrial-scale Bridgman facility in the Beijing Institute of Aeronautical Materials. Twelve rods were cast simultaneously with two rods per group, meaning that two rods shared one grain selector, as shown in Fig. 7. The SX alloy with ⟨0 0 1⟩ orientation was directionally solidified. A withdrawal rate of 5 mm/min was used, and the molten metal was poured under vacuum conditions at 1550 °C. The core was composed of silica-based material, while the shell consisted of alumina-silica-based material. The rods underwent standard heat treatment after casting, and a chemical etching process, with HCl/H_2O_2 as the etchant, was used to reveal whether RX had occurred.

Table 3
Nominal composition of alloy DD6.

Element	Ni	Cr	Co	Mo	W	Ta	Re	Nb	AL	Hf
wt.%	Balance	4.3	9	2	8	7.5	2	0.5	5.6	0.1

3.2. Mechanical testing for yield strength

To improve the accuracy of the simulation, hot compression tests were conducted to obtain the yield strength of the as-cast SX superalloy DD6. Cylindrical pieces with a diameter of 6 mm and a length of 10 mm were cut using electrical discharge machining (EDM) from the as-cast test bars of SX DD6 with a diameter of 15 mm and a length of 300 mm. Compressive testing was carried out with a thermo-mechanical tester (Gleeble 3500) at different temperatures and a strain rate of $10^{-4}\,s^{-1}$. Great care was taken to ensure that only test pieces within 10° of the ⟨0 0 1⟩ axis were employed for the compressive testing. For tests below 1000 °C, the pieces were heated at a rate of 15 °C/s, and once the target temperature was reached, it was held for 1 min before compression. For tests above 1000 °C, the heating rate was increased to 2 °C/s above 1000 °C. The holding time above 1000 °C was also 1 min. A vacuum was used to simulate the environment during investment casting. The yield strength data was extracted from the compression test results for modeling purposes. Typical stress–strain curves are shown in Fig. 8, and the variation of the flow stress with temperature for different SX superalloys is shown in Fig. 9. Panwisawas et al. (2013a,b) and Wang et al. (2009) provided the yield strength at different temperatures for the as-cast CMSX4 and as-heated SRR99, respectively. As can be seen, the flow stress of the as-cast DD6 is lower than that of the as-heated DD6.

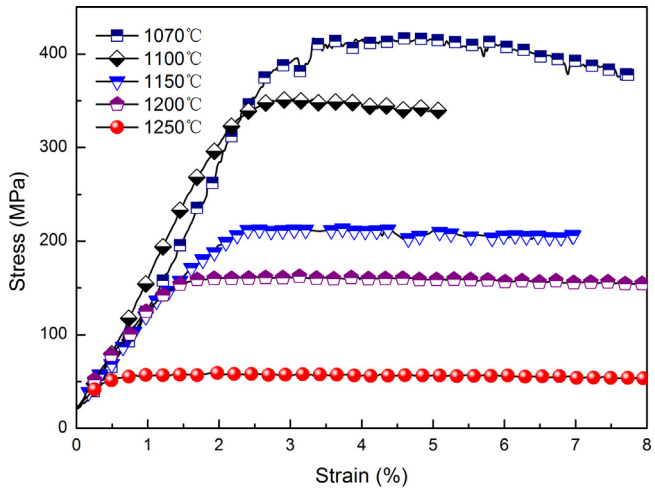

Fig. 8. Stress–strain curves at different temperatures for the as-cast DD6.

4. Modeling approach

Commercially available finite element method software (ProCAST and ABAQUS) was used to model the temperature and strains. Thermo-elastic–plastic analysis was carried out, with the high temperature plasticity assumed to be rate-independent. Temperature-dependent material parameters for the DD6 superalloy were assumed. The following thermo-physical properties of DD6 and the ceramic molds were used as isotropic parameters: density, specific heat capacity, thermal conductivity, and thermal expansion coefficient. The orthotropic mechanical properties of DD6 SX superalloy were considered using isotropic hardening criteria, including the elastic modulus, Poisson's ratio, yield stress, and ultimate yield strength. The stress, stored plastic energy, and strains, especially the plastic strains, were of primary interest. A 60° section of the whole model, with two test rods per group, was simulated because of its periodic symmetry. The interaction between the cores and shells was assumed to be free of friction during casting. It is supposed that cores and shells are connected. To model the shell and core, purely isotropic elastic properties were assumed. It should be noted that this hypothesis will lead to the prediction of larger stresses and strains because of the possible fracture of ceramic materials. This will be discussed later in this paper.

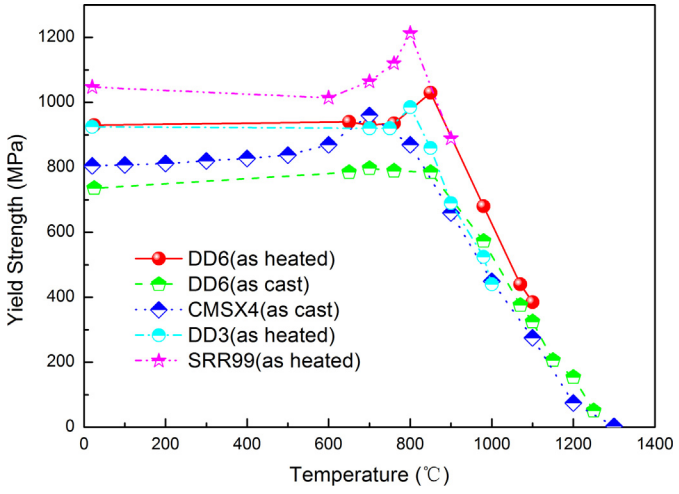

Fig. 9. Variation of yield strength of different SX Ni-based superalloys with temperature (as-cast DD6 from experiments; as-cast CMSX4, and as-heated SRR99, DD3 and DD6 from the literature).

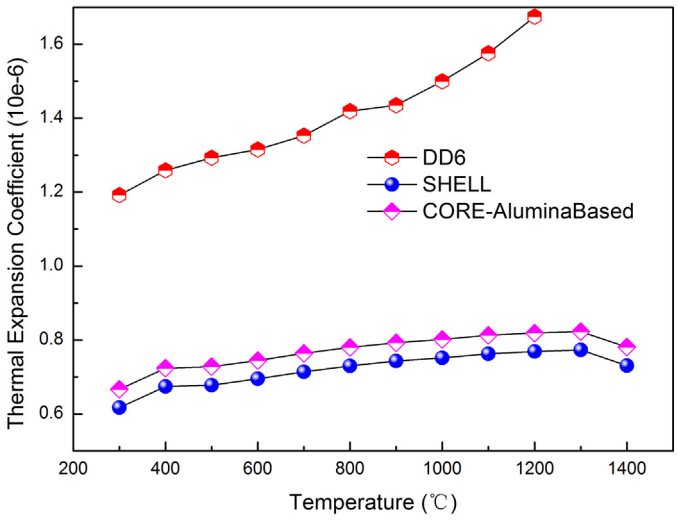

Fig. 10. Variation of thermal expansion coefficient of casting, shell and core with temperature (the reference temperature is 20 °C).

Ignoring high temperature creep strain, static equilibrium was assumed during the calculation of the stress field, which also ignored the cooling rate. The following equations are employed to determine the equivalent effective plastic strain and plastic dissipation energy, denoted $\bar{\varepsilon}_{pl}$ and U_{pl}, respectively. They take the following forms:

$$\bar{\varepsilon}_{pl} \equiv \int_0^{\bar{\varepsilon}_{pl}} d\bar{\varepsilon}_{pl} = \int \frac{\boldsymbol{\sigma} : d\boldsymbol{\varepsilon}_{pl}}{f(\boldsymbol{\sigma})} \tag{22}$$

$$dU^{pl} = \int_0^{\varepsilon_{pl}} \boldsymbol{\sigma} : d\varepsilon_{pl} \tag{23}$$

Thermal expansion coefficients are especially significant in this model, and therefore, temperature-dependent values were used, as illustrated in Fig. 10. Great care was taken to ensure that the mesh was sufficiently fine for the simulation results to be independent of element size. An explicit integration scheme was used, and the simulation results discussed below correspond to the integration points because of the high accuracy of these positions.

5. Influence of geometric features

Before presenting the comparison of the simulated and experimental results for the test pieces, the influence of typical geometric features on the induced plasticity was investigated first, with the results discussed below. Though the preliminary research was based on simple assumptions, some of which are unachievable in reality, the results may be helpful for understanding what causes plastic deformation and the subsequent RX.

5.1. Cored rods with uniform walls

This case was investigated to evaluate the plasticity induced by the ceramic core, which is analogous to the strain induced on the inner surface of a turbine blade. The diameter of the rod was 20 mm, and the rod axis was parallel to the casting crystallographic orientation ⟨0 0 1⟩ of the SX superalloy, as shown in Fig. 11(a). It was assumed that the superalloy and core maintain the same temperature and interact without friction during the solidification and subsequent cooling from 1370 °C to 70 °C. A quarter section of the cored rod model was simulated because of its four-fold crystallographic symmetry.

The rod casting wall thickness of 5 mm was chosen to investigate the evolution of stress and strain during solidification, and

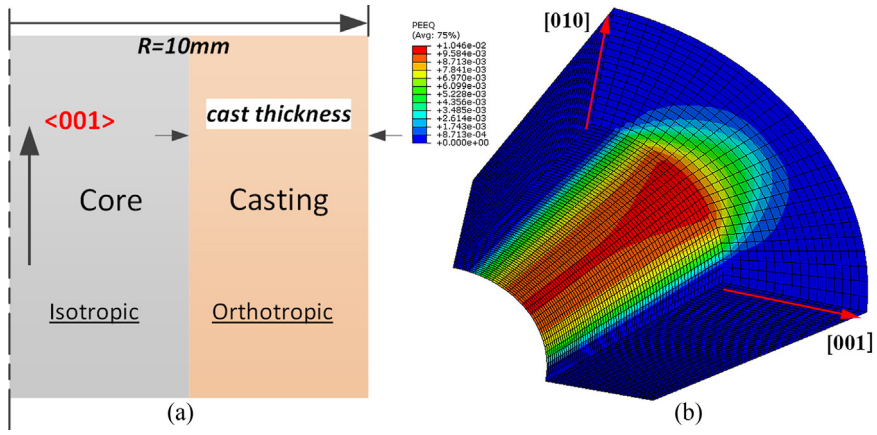

Fig. 11. Schematic of cored rod (a) and simulated equivalent effective plastic strain contour (b).

the modeled equivalent plastic strain contour results are illustrated in Fig. 11(b). The final distribution of plastic strain on the circumference of the rod is non-uniform, with the maximum values in the primary ⟨0 1 1⟩ orientation. This finding can be explained by the maximum Young's and shear moduli of the (0 0 1) plane being found in the ⟨0 1 1⟩ direction. Fig. 12 shows the variation of simulated plastic, elastic, and thermal strain, as well as the plastic dissipation energy density, with temperature during the solidification of the cored rod. The SX Ni-based superalloy undergoes plastic deformation easily at high temperatures, especially above 1000 °C, mainly because of the low yield strength. However, the plastic strain induced at this stage is usually smaller in scale compared with that below 800 °C, as illustrated in Fig. 12. This can be explained by comparing the variation of the potential function and yield strength with the temperature, as shown in Fig. 13. The potential function was calculated from Eq. (14); a material will yield when the potential function is larger than the yield strength. The evolution of plastic strain may play a role in the characteristic yield strength of SX superalloy DD6. As seen in Fig. 13, the yield strength of DD6 increases significantly to its peak value around 800 °C during solidification, but below 800 °C the yield strength undergoes a small decline and remains relatively unchanged until room temperature is reached. On the other hand, the thermal strain and stress increase continuously, as shown in Fig. 12, with the majority of plastic strain occurring below 800 °C. High equivalent plastic strain can be predicted without considering the fracture of the core. The plastic dissipation energy was also calculated, with only a small fraction needed to be stored in the material to act as the driving force for RX. According to classical theory, the driving force for RX in a deformed metal can be estimated with the following equation:

$$p = \frac{1}{2}\rho\mu b^2 \tag{24}$$

with ρ, μ, and b representing dislocation density, shear modulus, and Burger's vector length, respectively. A rough estimate of the driving force can be made for the superalloy. Assuming ρ is 10^{15} m^{-2}, μ is about 50 GPa, and b is 0.36 nm, then the driving force p = 1.25 MPa (1.8×10^6 J/m^3). This value is comparable to the calculated results, assuming about 2–5% plastic dissipation energy in the material.

The influence of different core/casting area ratios was investigated by changing the core's radius. As shown in Fig. 14, the thinner the casting wall, the larger the maximum equivalent plastic strain, meaning that RX is more likely to occur in thin-walled sections.

5.2. Decentralized-core rods

The wall thickness around the ceramic core is usually non-uniform for turbine blades. Therefore, decentralized-core rods were designed to simulate the influence of non-uniform wall thickness on the final plasticity. The diameters of rod and core were fixed at 20 mm and 10 mm, respectively, and the core deviated from

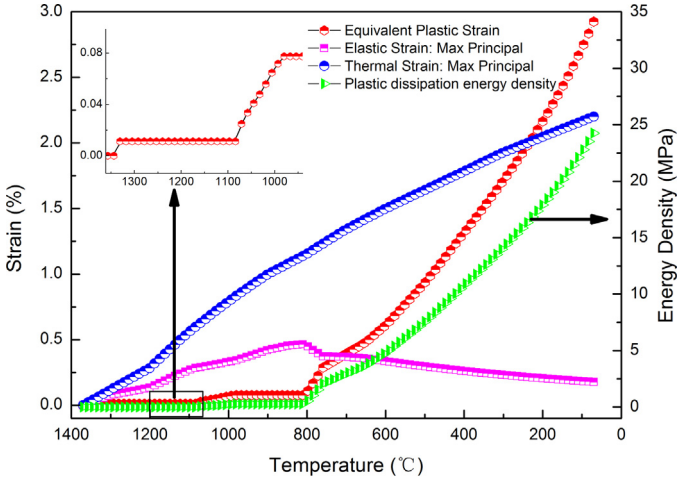

Fig. 12. Variation of simulated equivalent plastic strain, elastic strain, thermal strain, and plastic dissipation energy density with temperature during solidification.

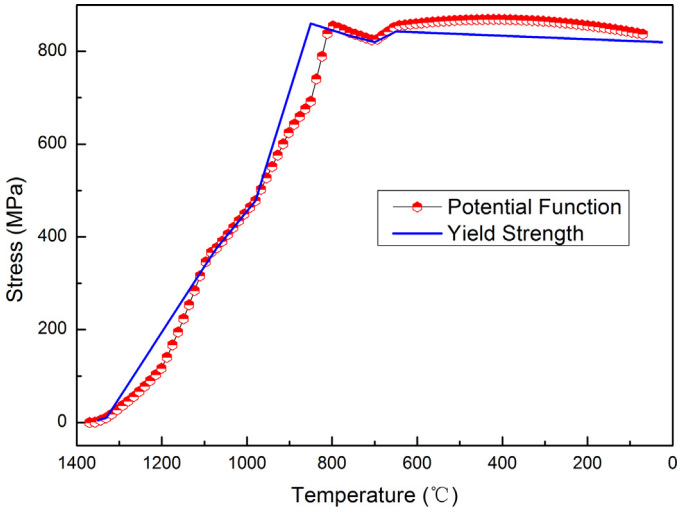

Fig. 13. Comparison of simulated potential function and experimental yield strength during solidification, indicating when plasticity occurs.

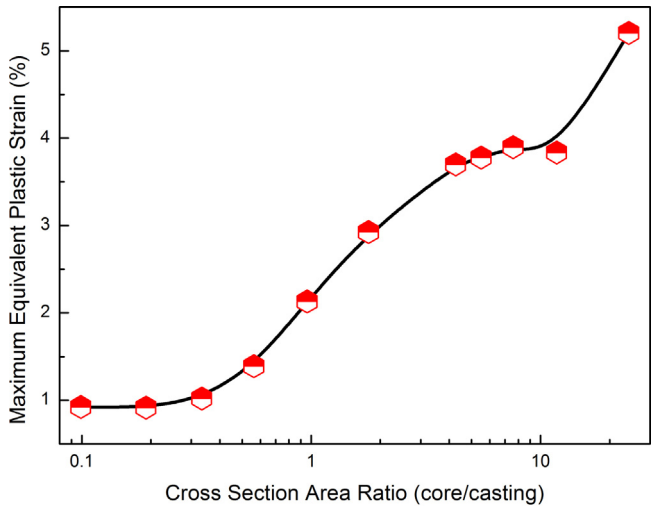

Fig. 14. Variation of maximum equivalent plastic strain with the area ratio (core/casting).

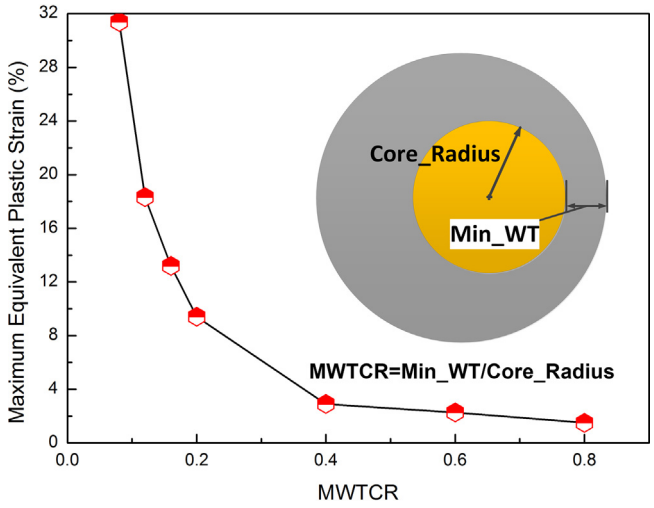

Fig. 16. Variation of maximum equivalent plastic strain with the parameter MWTCR.

the center at varied distances. The remaining simulation conditions were the same as those for the first case. Only half of the model was simulated because of the geometric symmetry. The correlation between maximum plastic strain and wall thickness was studied, with the parameter minimum wall thickness/core radius (MWTCR) used for convenience. The zone of maximum plasticity is influenced by the material's crystallographic orientation and MWTCR, as illustrated in Fig. 15. When MWTCR is large, meaning the wall thickness around the core is relatively uniform, plasticity is prone to occur in the zone approaching the ⟨0 1 1⟩ direction on the circumference. Otherwise, the area of maximum plasticity corresponds to the area with the thinnest wall. Fig. 16 confirms that the smaller MWTCR is, the larger the value of maximum equivalent plastic strain obtained. If the direction of the thinnest wall coincides with the ⟨0 1 1⟩ direction, the plasticity will reach its peak value. This may explain why the degree of irregularity of the wall thickness has a more significant influence on the final plasticity than elastic anisotropy. Concerning the solidification process, much higher plastic strains are found at temperatures of 1000 °C or above (Fig. 17), which means more damage occurs compared to the uniform simulation if the same plasticity is induced. This suggests that fabricating components with uniform wall thickness helps prevent RX.

5.3. Rods with changing cross-sections

This case was designed to simulate the mechanical constraints of flanges provided by platforms and shrouds in real turbine blades. Twelve castings were produced with the industrial Bridgman

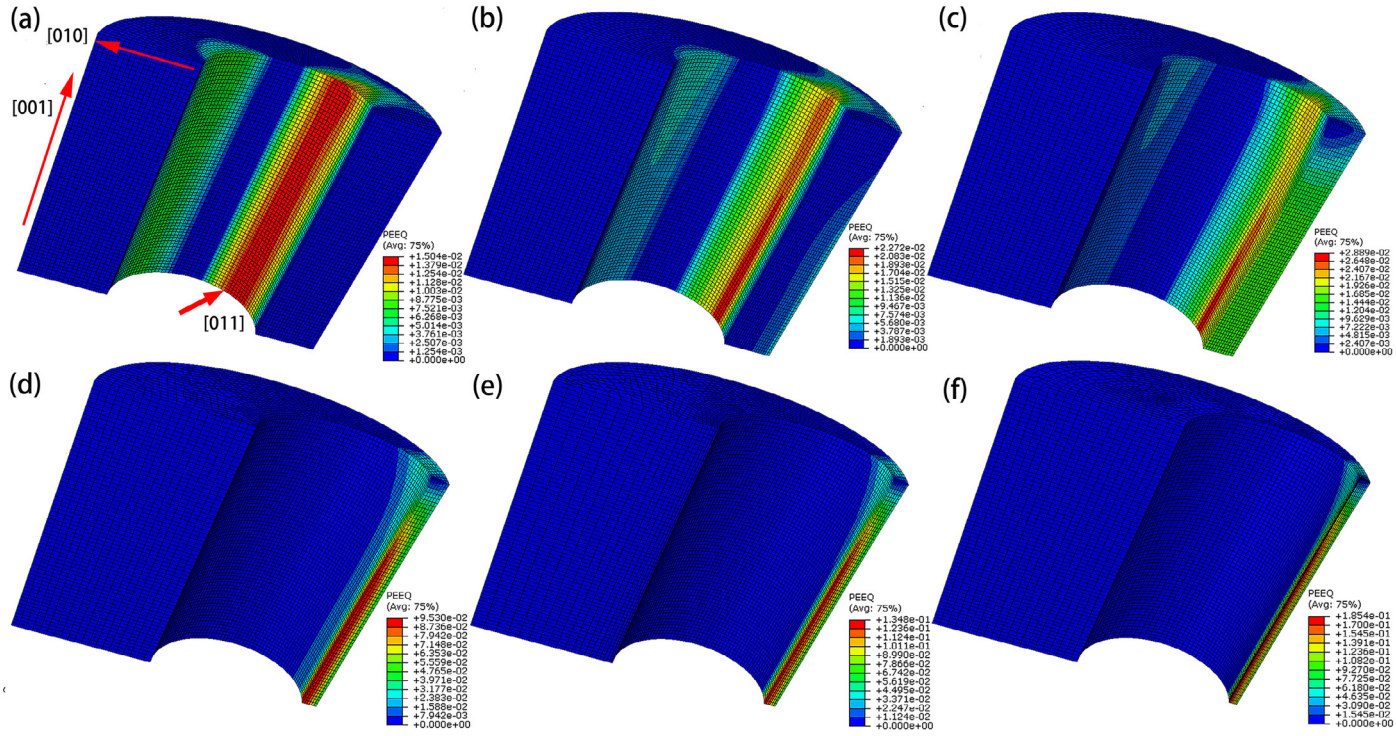

Fig. 15. Contour maps of the final plasticity of different cases with various offset distances: (a) 1 mm; (b) 2 mm; (c) 3 mm; (d) 4 mm; (e) 4.2 mm; (f) 4.4 mm.

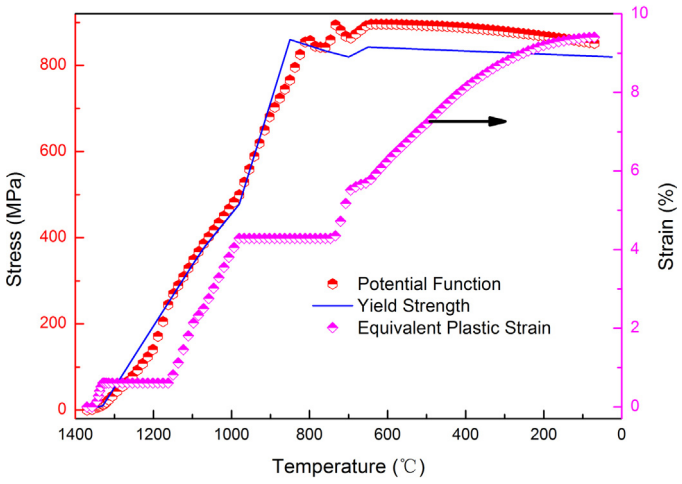

Fig. 17. Variation of simulated equivalent plastic strain, potential function, and yield strength with temperature during solidification (for the case of a 4 mm-offset core).

directional solidification method to make the process as close as possible to actual working conditions. The nominal withdrawal rate was 5 mm/min. The rotational axes of the test rods were parallel to the ⟨0 0 1⟩ direction, like the first two cases. Fig. 18(a) shows the geometric details of the test rods, excluding the runner system and grain selector. The top and bottom sections are cylinders 10 mm in diameter and 20 mm in length. The length of the middle part, the most pertinent part for this case, is 40 mm, and the diameter varies from 4 mm to 18 mm so that the effect of the cross-section ratio (small section/large section) could be investigated. The nominal shell thickness is 5 mm. The reason for induced plastic strains is illustrated in Fig. 18(b). The middle part should bear tension stress because of the smaller thermal expansion coefficients of the ceramic-based shell compared to the cast. In addition, the temperature at the top of the middle part is relatively higher, resulting in lower yield strength. Therefore, plastic deformation will most likely occur in the region where the cross-section abruptly increases.

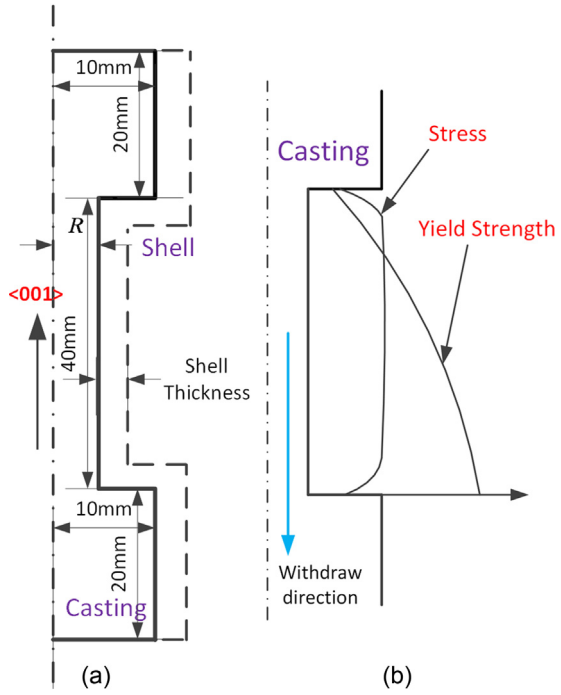

Fig. 18. Geometric details of a varying cross-section rod (a) and comparison between stress and yield strength of the middle part (b).

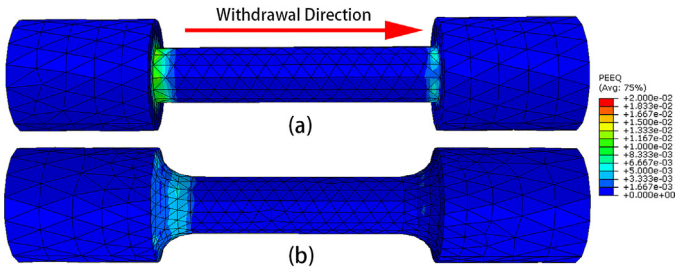

Fig. 19. Comparison of equivalent plastic strain contours between changing cross-section rods without filets (a) and with filets (b) (section ratio is 0.25).

Rods without filets of different section ratios were simulated first. The simulation results confirm the above analysis, as shown in Fig. 19(a). The maximum equivalent plastic strain is affected by the stress concentration at sharp corners and tensile stress of the part with the smaller section. The bottom part yields mainly because of the stress concentration. The former factor plays a more dominant role when the section ratio becomes larger, while the latter becomes more important if the section ratio is small. The minimum plastic strain is achieved when the section ratio lies between 0.2 and 0.5, giving a value of approximately 2%, as illustrated in Fig. 20. However, even this level of plasticity can give rise to RX during the subsequent heat treatment. Therefore, filets should be introduced to avoid large levels of plasticity during solidification and the subsequent RX induced by section variation. The rod with a section ratio of 0.25 and filets was then simulated to verify this point. The result (Fig. 19(b)) shows that the maximum plastic strain (0.71%) is about only one-third compared to that of the rod of the same section ratio without filets (1.96%). Therefore, filets should be added to the sites with changing cross-sections in a turbine blade aerofoil to avoid RX. These kinds of sites include the joints between platform and blade, as well as leading (trailing) edges in a hollow blade. Combined with the second case modeled, another conclusion is that the geometric features are more significant than a material's orientation to the plasticity induced by the investment casting process.

In addition, the effect of shell thickness, which was varied from 3 mm to 9 mm, was studied. The 0.25 section-ratio rods without filets were used in the simulation. Unexpectedly, the maximum plastic strain had no obvious correlation with shell thickness, and varied from 1.0% to 2.4%. By comparing these cases, a primary

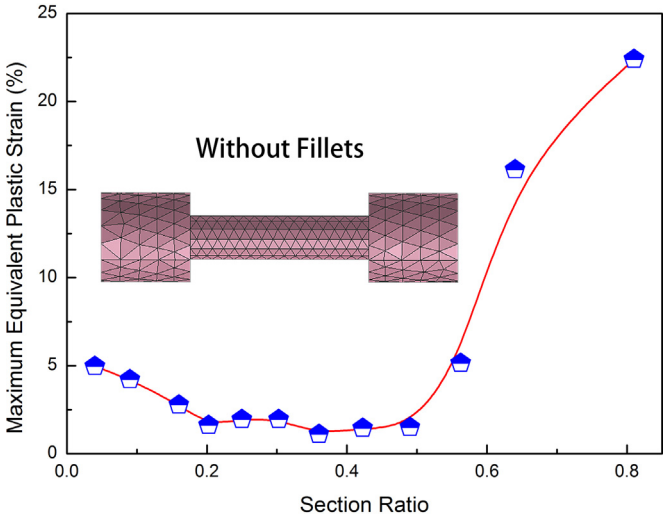

Fig. 20. Variation of maximum equivalent plastic strain with section ratio.

Fig. 21. Test bars with buckled cores: (a) core does not penetrate the wall; (b) core penetrates the wall; (c) RX grains (marked with closed red lines) in test pieces with penetrating core. (For interpretation of the references to color in this figure caption, the reader is referred to the web version of this article.)

conclusion may be drawn; the influence of ceramic cores on plastic strain is more significant than that of the shell.

6. Comparison of models and experiments

Over 100 cored cross-section rods were fabricated with the Bridgman directional solidification method. It was found that the ceramic cores often buckled or broke during the preheating and casting processes, causing non-uniform wall thickness or the core to penetrate the wall (Fig. 21(a) and (b)). RX occurred in most of the core-penetrated rods (Fig. 21(c)), while little RX grains were found in the other rods, especially in normal cored rods. Interestingly, almost all of the RX grains appear below the holes as opposed to around the holes. To some extent, these findings were consistent with the simulation results (shown in Fig. 22). In the normal test bars, only a maximum of 6% effective plastic strain is predicted in the upper changing cross-section zone. For the test pieces with buckled cores, nearly 30% effective plastic strain is predicted in the zone below the hole, meaning that this zone will be more prone to RX during the subsequent heat treatment. This can be easily understood in the context of the case in Section 5.2. The zone below the hole is representative of a place with small MWTCR, which has the highest plastic strain. In this situation, the material orientation will also influence the final maximum plastic strain, which has been demonstrated by the previous simulations. It should be noted that most holes formed on the upper half of the middle part of the experimental samples because of their geometric characteristics. Thus, the area beneath the hole is thinner than the area above. Occasionally, the holes formed in the lower half of the middle part. In these cases, according to the models and the above analysis, RX grains should appear above the hole, which was confirmed by the experimental samples (the far right rod in Fig. 21(c)). Thus, RX is likely to occur at the thin-walled sites below or above the hole instead of around the hole.

It should be pointed out that high plastic strains are predicted in zones A and B (see Fig. 22(b)), where RX was not found. This can be explained by the following. First, the model is not a perfect replica of the real test pieces, giving rise to the differences found. These situations are difficult to completely describe in the model. Besides, higher plastic strains in some zones will be predicted because the fracturing of the core and shell was ignored.

Most of the plastic strain occurs above 1000 °C for the normal test pieces (shown in Fig. 23), which is different from the case in Section 5.1. The zone with both changing cross-section and core is more prone to RX, and should be carefully treated during the manufacturing of SX components. The effect of core material on plasticity was also investigated with the model. Two distinct core systems were simulated: an alumina-based core (Core 1) and a silica-based core (Core 2). Though Core 1 was appreciably stiffer than Core 2, a little more plastic strain was induced within the metal cast around Core 2 than Core 1 because of the smaller thermal expansion

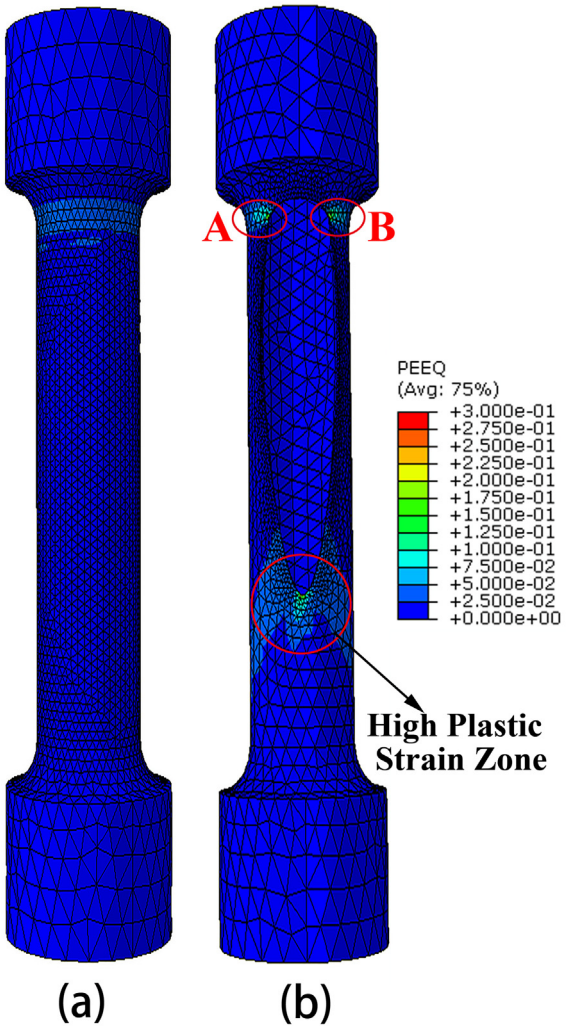

Fig. 22. Distribution of predicted effective plastic strains in normal (a) and core-buckled test pieces (b).

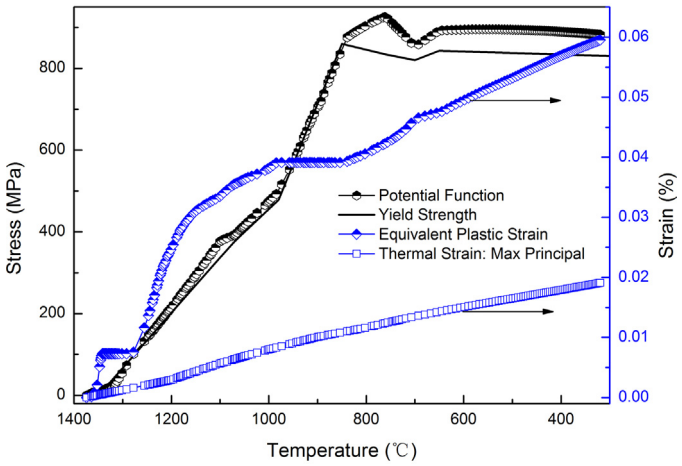

Fig. 23. Variation of potential function, equivalent plastic strain, and thermal strain with temperature (at the maximum integration point for normal test pieces with alumina cores and 1 mm wall thickness).

coefficient of Core 2. Besides, the predicted plastic strains were very close between the two cores modeled, meaning that the effect of core material is less than that of geometric features when casting. In addition, the silica-based core can be leached out of the casting easily, leading to its employment in most situations.

Finally, it should be mentioned that the predicted plastic strains in this research may be larger than in reality. One of the reasons is that the shell and core were treated as ideal elastic materials, which ignores fracturing during the casting process. Evidence for this is that the core and shell usually underwent abnormally high stress during modeling. This can explain why RX was not found in certain areas of the normal cored rods fabricated, while the predicted plastic strain was as high as 6%. Therefore, the model presented in this research is only capable of predicting the sites of high plasticity, or in other words, it is only semi-quantitative.

7. Conclusions

A macroscopic, phenomenon-based, thermo-elastic–plastic model for the processing-induced plasticity during investment casting has been developed. Though only semi-quantitative, the model is capable of predicting the sites where localized plasticity can induce recrystallization during the heat treatment of single crystal superalloy castings. The following conclusions can be drawn.

(1) From an engineering perspective, orthotropic elastic properties and Hill's yield criterion can be employed in the thermo-mechanical modeling of single crystal nickel-based superalloys.
(2) The influence of ceramic cores on plastic strain is more significant than the shell. The thin-walled sections have an increased propensity for recrystallization.
(3) The geometric features are more significant than material orientation and material type. Filets should be introduced at the sites with abrupt changes of cross-section to avoid recrystallization.
(4) The thin-walled sites below or above the holes (along the withdrawal direction) have an increased propensity for recrystallization.

Acknowledgements

This research was funded by the National Basic Research Program of China (No. 2011CB706801) and National Natural Science Foundation of China (No. 51171089 and No. 51374137).

References

Bayerlein, U., Sockel, H.G., 1992. Determination of single crystal elastic constants from DS- and DR-Ni-based superalloys by a new regression method between 20 °C and 1200 °C. In: Antolovich, S.D., Stusrud, R.W., Mackay, R.A., Anton, D.L., Khan, T., Kissinger, R.D., Klarstrom, D.L. (Eds.), Superalloys. Warrendale, pp. 695–704.
Burgel, R., Portella, P.D., Preuhs, J., 2000. Recrystallization in single crystals of nickel base superalloys. In: Pollock, T.M., Kissinger, R.D., Bowman, R.R., Green, K.A., Mclean, M., Olson, S., Schirra, J.J. (Eds.), Superalloys. Warrendale, pp. 229–238.
Dahlen, M., Winberg, L., 1980. Influence of gamma'-precipitation on the recrystallization of a nickel-base super-alloy. Acta Metall. 28 (1), 41–50.
Dai, H.J., Dong, H.B., D'Souza, N., Gebelin, J.C., Reed, R.C., 2011. Grain selection in spiral selectors during investment casting of single-crystal components: Part II. Numerical modeling. Metall. Mater. Trans. A 42A (11), 3439–3446.
Ding, Z.P., Liu, Y.L., Yi, Z.Y., Yang, Z.G., Cheng, X.M., 2004. Elastic–plastic constitutive model of fcc single crystal materials. J. Cent. South Univ. Technol. 35 (3), 423–428.
Fahrmann, M., Fahrmann, E., Pollock, T.M., 1999. Determination of matrix and precipitate elastic constants in (γ–γ′) Ni-base model alloys, and their relevance to rafting. Mater. Sci. Eng. A 260 (1–2), 212–221.
Green, D.J., 1998. An Introduction to the Mechanical Properties of Ceramics, first ed. Cambridge University Press, Cambridge, UK, pp. 13–69.
Hermann, W., Han, J., 1996. Elastic properties and determination of elastic constants of nickel-base superalloys by a free-free beam technique. In: Kissinger, R.D., Deye, D.J., Anton, D.L., Cetel, A.D., Nathal, M.V., Pollock, T.M., Woodford, D.A. (Eds.), Superalloys. Warrendale, pp. 229–238.
Meng, J., Jin, T., Sun, X.F., Hu, Z.Q., 2010. Effect of surface recrystallization on the creep rupture properties of a nickel-base single crystal superalloy. Mater. Sci. Eng. A 527 (23), 6119–6122.
Moverare, J.J., Johansson, S., Reed, R.C., 2009. Deformation and damage mechanisms during thermal–mechanical fatigue of a single-crystal superalloy. Acta Mater. 57 (7), 2266–2276.
Pan, D., Xu, Q., Liu, B., Li, J., Yuan, H., Jin, H., 2010. Modeling of grain selection during directional solidification of single crystal superalloy turbine blade castings. J. Miner. Met. Mater. Soc. (JOM) 62 (5), 30–34.
Panwisawas, C., Gebelin, J.C., Reed, R.C., 2013a. Analysis of the mechanical deformation arising from investment casting of directionally solidified nickel-based superalloys. Mater. Sci. Technol. 29 (7), 843–853.
Panwisawas, C., Mathur, H., Gebelin, J., Putman, D., Rae, C.M.F., Reed, R.C., 2013b. Prediction of recrystallization in investment cast single-crystal superalloys. Acta Mater. 61 (1), 51–66.
Reed, R.C., 2006. The Superalloys: Fundamentals and Applications, first ed. Cambridge University Press, New York, pp. 33–120.
Wang, L., Xie, G., Lou, L.H., 2013. Effect of carbon content on the recrystallization of a single crystal nickel-based superalloy. Mater. Lett. 109, 154–157.
Wang, L.N., Liu, Y., Yu, J.J., Xu, Y., Sun, X.F., Guan, H.R., Hu, Z.Q., 2009. Orientation and temperature dependence of yielding and deformation behavior of a nickel-base single crystal superalloy. Mater. Sci. Eng. A 505 (1–2), 144–150.
Wu, Y.X., Yang, R.B., Li, S.S., Ma, Y., Gong, S.K., Han, Y.F., 2012. Surface recrystallization of a Ni_3Al based single crystal superalloy at different annealing temperature and blasting pressure. Rare Metals 31 (3), 209–214.
Xie, G., Wang, L., Zhang, J., Lou, L.H., 2012. Orientational dependence of recrystallization in a Ni-base single-crystal superalloy. Scripta Mater. 66 (6), 378–381.
Xiong, J.C., Li, J.R., Liu, S.Z., Zhao, J.Q., Han, M., 2010. Effects of carburization on recrystallization behavior of a single crystal superalloy. Mater. Charact. 61 (7), 749–755.
Zambaldi, C., Roters, F., Raabe, D., Glatzel, U., 2007. Modeling and experiments on the indentation deformation and recrystallization of a single-crystal nickel-base superalloy. Mater. Sci. Eng. A 454, 433–440.